SOILS AND FOUNDATIONS Vol. 48, No. 5, 693–711, Oct. 2008
Japanese Geotechnical Society

NUMERICAL SIMULATION OF MODEL TESTS OF PIER-SHALLOW FOUNDATION SYSTEMS SUBJECTED TO EARTHQUAKE LOADS USING AN ELASTO-UPLIFT-PLASTIC MACRO ELEMENT

Masahiro Shirato[i], Roberto Paolucci[ii], Tetsuya Kouno[iii], Shoichi Nakatani[iv], Jiro Fukui[v], Roberto Nova[vi] and Claudio di Prisco[vi]

ABSTRACT

A dynamic analysis model for the nonlinear behavior of a shallow foundation subjected to seismic loads is developed. A macro-element approach is revised assuming elasto-uplift-plastic behavior, in which uplifting and coupling effects of vertical, horizontal, and moment loads are taken into account. Large-scale shake table experiments of model pier footings are also conducted and simulated using the revised macro-element model. The numerical result reveals that the shape of the hysteresis loops for coupled load-displacement relationships is predicted very well, including the effects of uplift. In addition, the revised model can account for settlement with some inclination that has accumulated during the excitation.

Key words: macro-element, numerical simulation, shake table test, shallow foundation (**IGC**: E12/E14/H1)

INTRODUCTION

Previous large earthquakes in Japan have shown no harmful damage to highway bridge shallow foundations such as settlements or rotations. Experimental evidence has also shown that, even though the factor of safety in terms of bearing capacity reaches unity several times during seismic excitations, failure is not necessarily indicated (Shirato et al., 2008). Rather, experimental results indicate that the accumulation of permanent displacement during earthquakes should be considered when the seismic performance of a shallow foundation is assessed. Therefore, a method by which to estimate permanent displacements is needed.

To develop such a numerical model for shallow foundations, there are two crucial points to be taken into account. First, during large earthquakes, typical highway bridge shallow foundations are likely to be partially uplifted as the rocking increases. This induces, for example, the initiation of large rotations, the occurrence of hysteresis between combined loads and displacements, and the elongation of vibration characteristics. A survey of twenty design case histories of highway bridge shallow foundations in Japan has revealed that the ratios of the bearing capacities to the dead loads ranges from 9.0 to 24.0. Furthermore, a technical report by the Public Works Research Institute, Tsukuba, Japan (PWRI) has indicated that, in early design case histories, the lateral seismic intensity coefficients at which highway bridge shallow foundations initiate the rocking-induced uplift ranged from 0.07 to 0.25 (Fukui et al., 1999). The reason for this is that the Specifications for Highway Bridges (Japan Road Association, 2002), which describes the highway bridge design norm in Japan, have required further empirical regulations for normal and small-to-mid scale earthquake designs, in addition to principle checks for the bearing capacity, sliding, and tilting/overturning. For example, the choice of bearing layer, the maximum soil reaction stress intensity, and the maximum degree of partial uplift are limited to prevent excessive settlement of the foundations.

Furthermore, irreversible settlements are not only caused by vertical forces but also by rocking. Large vertical stresses due to the rocking behavior of shallow foundations are likely to be transferred to the soil beneath the footing, especially at the corners of the footing. Therefore, the coupling effects of vertical forces and moments must be taken into account in order to estimate the ir-

[i] Senior Researcher, Center for Advanced Engineering Structural Assessment and Research, Public Works Research Institute, Ibaraki, Japan (shirato@pwri.go.jp).
[ii] Associate Professor, Dipartimento di Ingegneria Strutturale, Politecnico di Milano, Italy.
[iii] Researcher, Center for Advanced Engineering Structural Assessment and Research, Public Works Research Institute, Japan.
[iv] Chief Researcher for Management System and Substructures, Center for Advanced Engineering Structural Assessment and Research, Public Works Research Institute, Japan.
[v] Advanced Construction Technology Center, Tokyo, Japan.
[vi] Professor, Dipartimento di Ingegneria Strutturale, Politecnico di Milano, Italy.
The manuscript for this paper was received for review on November 21, 2007; approved on July 16, 2008.
Written discussions on this paper should be submitted before May 1, 2009 to the Japanese Geotechnical Society, 4-38-2, Sengoku, Bunkyo-ku, Tokyo 112-0011, Japan. Upon request the closing date may be extended one month.

reversible settlement of the footing, even though, in practice, the footing-soil interaction is assumed to be linear elastic and the rocking-induced settlement is assumed to be negligible as long as the footing meets other design norms.

Accordingly, the present study scrutinizes the effectiveness of the macro element approach to predict the seismic behavior of shallow foundations during large earthquakes. In particular, the present study implements a model of the uplift behavior of shallow foundation into a typical elasto-plastic macro element. The modeling of the uplift behavior is performed using a model described in the Japanese Specifications for Highway Bridges (Japan Road Association, 2002) and experimental observations of a pier-shallow foundation systems subjected to cyclic lateral loads that is examined in a companion paper (Shirato et al., 2008).

Note that the FORTRAN source code used for the calculations in the present paper are described in a report by the Public Works Research Institute, Tsukuba, Japan (PWRI) (Nakatani et al., 2008).

THEORETICAL BACKGROUND

Hereinafter, the behavior of the footing is expressed as shown in Fig. 1, where V, H, and M are the vertical force, horizontal force, and moment at the base center of the footing, v, u, and θ are the corresponding vertical displacement, horizontal displacement, and rotation at the same position, and B is the footing length. The forces and displacements in Fig. 1 are in the positive directions, where the positive direction of rotation, θ, is clockwise.

Uplift on an Elastic Medium

As described above, the partial uplift of the footing is expected to occur easily during earthquakes. During the uplift, a progressive reduction in the contact area of the footing with the soil can be expected, which results in a nonlinear relationship between the moment and rotation of the footing. Experimental results (Shirato et al., 2008) also reveal that the uplift behavior influences the foundation response during large earthquakes, including the shape of hysteresis loops between loads and displacements.

The advent of the seismic design of highway bridge shallow foundations that positively considers the reduction in the seismic force to the footing arising from the uplift of footing was first applied in the Honshu-Shikoku Bridges project, the world longest bridges connecting the main Honshu island and the Shikoku island in Japan, (e.g., Honshu-Shikoku Bridge Authority, 1990). Then, in 1996, the Japanese Specifications for Highway Bridges (Japan Road Association, 2002) also introduced such a reduction in the seismic force to the footing in the structural design of shallow foundations for large earthquakes.

In the following, for example, the structural design of the footings of a rectangular shallow foundation for large-scale earthquake design in the Japanese Specifications for Highway Bridges will be summarized. A nonlinear rocking moment-rotation curve is calculated using a Beam-on-Winkler Foundation model that considers the partial uplift of the footing. Figure 2 shows a typical moment-rotation curve, where M_0 and θ_0 are the moment (kN·m) and rotation angle (rad) at the initiation of uplift, respectively:

$$M_0=(BV)/6, \quad \theta_0=(12M_0)/(B^3\cdot D\cdot k_v) \tag{1}$$

where V is the vertical force (kN), B is the footing length in the direction of the considered seismic excitation (m), D is the footing width (m), and k_v is the vertical subgrade reaction coefficient (kN/m^3). Design calculations generally assume that the vertical force, V, remains constant and equal to the dead load, V_0, as the first approximation, although, in reality, the vertical inertial force can be generated by the rocking-induced up-and-down movement at the center of gravity of the footing. The M-θ relationship is linear in the range $M \le M_0$, and becomes nonlinear in the range $M > M_0$:

$$M=M_0(\theta/\theta_0) \quad \text{if } M\le M_0, \tag{2}$$

$$M=M_0\,(3-2\sqrt{\theta_0/\theta}) \quad \text{if } M>M_0 \tag{3}$$

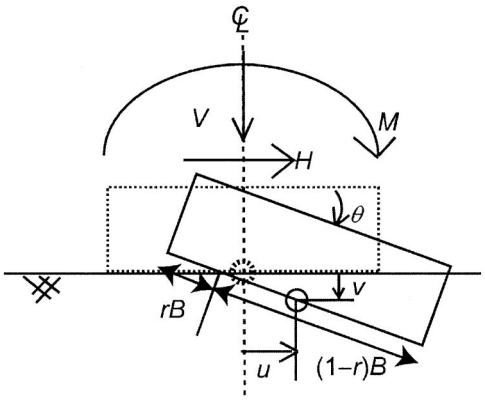

Fig. 1. Load and displacement vectors of footing

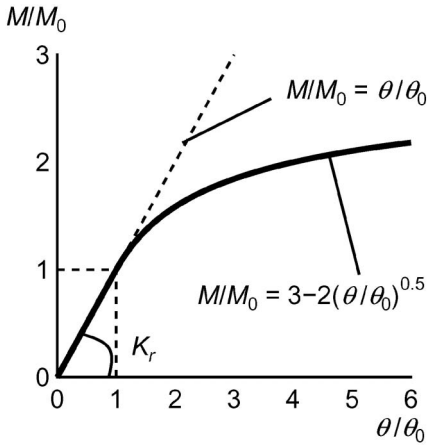

Fig. 2. Moment-rotation (M-θ) curve of shallow foundation considering uplift

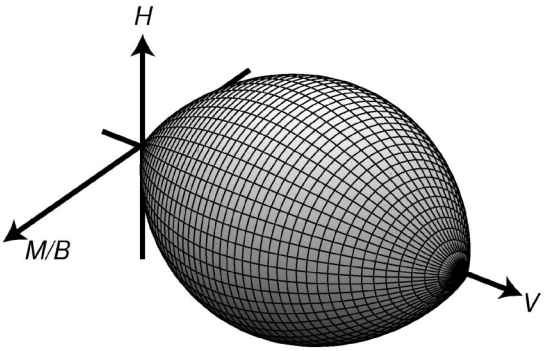

Fig. 3. Schematic diagram of bearing capacity surface

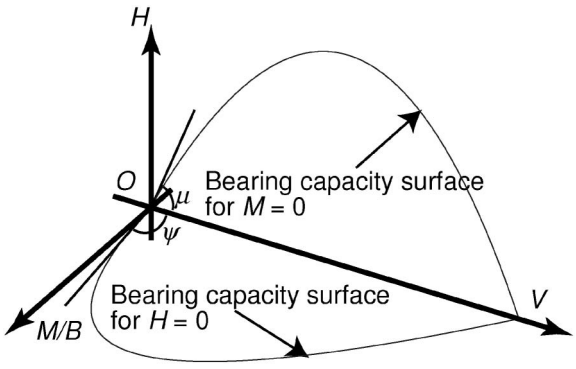

Fig. 4. Cross-sections of bearing capacity surface at $M=0$ and $H=0$

The energy conservation rule is then used to estimate the applied moment to the footing, so that the intensity and position of the reaction force normal to the footing base can be obtained. The bending moment and shear capacities of the cross-section of the footing are then checked.

Bearing Capacity Surface

Recent experimental results have shown that the bearing capacity of a footing with respect to combined loads can be approximated with a function in the *V-H-M/B* space, as shown in Fig. 3, where V is the vertical force at the base center of the footing, H is the horizontal force at the base center of the footing, and M/B is the rotational moment around the base center of the footing, normalized by the footing length B. The bearing capacity surface can usually be approximated by a rugby ball shaped function in the *V-H-M/B* space. For example, Nova and Montrasio (1991) expressed the bearing capacity surface for sand as follows:

$$f_{cr} = h^2 + m^2 - \xi^2(1-\xi)^{2\zeta} = 0 \tag{4}$$

where $h = H/(\mu V_m)$, $m = M/(\psi B V_m)$, $\xi = V/V_m$, and V_m is the bearing capacity in terms of centered vertical loading. Figure 4 illustrates the cross-sections on the $M=0$ and $H=0$ planes and a physical understanding of parameters, μ and ψ. Parameters μ and ψ are the tangents at the origin on the *V-H* and *V-M* planes, respectively. When $M=0$, $H=\mu V$ holds at the origin, i.e., sliding resistance. Accordingly, $\mu = \tan\phi$ or other values given in design codes can be employed, where ϕ is the shear resistant angle of the soil. ψ is associated with the bearing capacity under eccentric loading and is considered to take values of 0.33–0.48 (Nova and Montrasio, 1991): 0.33 is selected for Meyerhof's bearing capacity theory (1953) and 0.48 is selected for Vesic's correction (1991). ζ is also a parameter specifying the shape of the failure surface, for which Nova and Montrasio (1991) recommended $\zeta = 0.95$.

At present, it is suggested that the difference in the shapes of the bearing capacity surface is small (Shibata and Sekiguchi, 1995; Okamura et al., 2002). Accordingly, Eq. (4) accounts for a first approximation of the ultimate load combinations for any footing shape, although it was originally proposed for strip footings.

Macro Element Theory

Although the bearing capacity surface reveals the ultimate force equilibrium of a footing, it is not related to the mobilized inelastic displacement. The macro element theory has been established to express the evolution of plastic flow of inelastic displacement (Nova and Montrasio, 1991; Motrasio and Nova, 1997; Gottardi and Butterfield, 1995; Houlsby and Martin, 1993; Okamura and Matsuo, 2002; Paolucci, 1997).

The macro-element theory models the footing-underlying soil system as a unique element and describes its behavior within the context of work-hardening plasticity. Let us simply consider isotropic hardening. As the combined loads increase, the yield surface, which is homothetic in terms of the defined bearing capacity surface, expands inside the bearing capacity surface in the *V-H-M/B* space, and the corresponding combined irreversible displacements, v, u, and $B\theta$, evolve. Ultimately, the yield surface reaches the bearing capacity surface and the macro element becomes perfectly plastic. Since the underlying soil is not elastic even at small displacement levels and the elastic deformation may be negligible compared to the plastic deformation as the first approximation, this theory is considered to work well. Many case studies have proven that the macro-element theory works well for monotonic loading cases (Nova and Montrasio, 1991; Motrasio and Nova, 1997; Gottardi and Butterfield, 1995).

The application of an elasto-perfectly plastic macro element to seismic problems was pioneered by Paolucci (1997). Cremer et al. (2001, 2002) revised a macro element for a footing on a cohesive soil and showed an example of the computation of the seismic behavior of a bridge pier having a shallow foundation. The model of Cremer et al. is very sophisticated with respect to kinematic hardening and uplift behavior, but is somewhat cumbersome with respect to computer-coding. However, the most salient problem is that, with the exception of a study by Okamura and Matsuo (2002), who compared a centrifuge shake-table experimental result for a retaining wall supported by a shallow foundation with a numerical simulation using their elasto-perfectly plastic macro element, little experimental calibration has been conducted. However, in the experiment of Okamura

and Matsuo, the effect of horizontal load on the footing response overwhelmed the effects of the other load components, resulting in the predominance of one-sided sliding.

SUMMARY OF THE PROPOSED ELASTO-UPLIFT-PLASTIC MACRO ELEMENT

In this section, the key ideas to assemble the above theories as a new macro element will be summarized. As shown in Fig. 1, the vectors of the combined loads transmitted from the superstructure to the base center of the footing, $\boldsymbol{F}$, and the displacements at the base center of the footing, $\boldsymbol{x}$, are expressed by

$$\boldsymbol{F}=(V\ H\ M)^{\mathrm{T}},\quad \boldsymbol{x}=(v\ u\ \theta)^{\mathrm{T}} \tag{5}$$

where the superscript T stands for transposition. Again, the loads and displacements in Fig. 1 are in the positive directions.

The present paper follows a typical macro element theory, describing the behavior of a footing-soil system within the context of strain hardening plasticity theory. The total incremental displacement of the footing, $\mathrm{d}\boldsymbol{x}$, is decomposed into two parts, elastic and plastic parts, $\mathrm{d}\boldsymbol{x}^{\mathrm{el}}$ and $\mathrm{d}\boldsymbol{x}^{\mathrm{pl}}$, respectively.

$$\mathrm{d}\boldsymbol{x}=\mathrm{d}\boldsymbol{x}^{\mathrm{el}}+\mathrm{d}\boldsymbol{x}^{\mathrm{pl}} \tag{6}$$

The incremental displacement ($\mathrm{d}\boldsymbol{x}$) and force ($\mathrm{d}\boldsymbol{F}$) relationship for each displacement component can be expressed using compliances $\boldsymbol{D}^{\mathrm{el}}$ and $\boldsymbol{D}^{\mathrm{pl}}$ as follows:

$$\mathrm{d}\boldsymbol{x}^{\mathrm{el}}=\boldsymbol{D}^{\mathrm{el}}\mathrm{d}\boldsymbol{F} \tag{7}$$
$$\mathrm{d}\boldsymbol{x}^{\mathrm{pl}}=\boldsymbol{D}^{\mathrm{pl}}\mathrm{d}\boldsymbol{F} \tag{8}$$

where each compliance consists of 3×3 components. Finally, the total incremental displacement-force relationship is derived as:

$$\mathrm{d}\boldsymbol{x}=(\boldsymbol{D}^{\mathrm{el}}+\boldsymbol{D}^{\mathrm{pl}})\mathrm{d}\boldsymbol{F} \tag{9}$$

The inverse of this equation gives the stiffness matrix for the macro element, $\boldsymbol{C}$.

$$\mathrm{d}\boldsymbol{F}=\boldsymbol{C}\,\mathrm{d}\boldsymbol{x}, \tag{10}$$
$$\boldsymbol{C}=(\boldsymbol{D}^{\mathrm{el}}+\boldsymbol{D}^{\mathrm{pl}})^{-1} \tag{11}$$

This matrix is hereinafter referred to as the elasto-plastic macro element. One of the advantages of the use of macro element is that the dimension of the stiffness matrix is very small, 3×3, so that macro elements will not become a large burden on the overall structural model.

However, as described above, even though the underlying soil is a linear elastic medium and no irreversible deformation is accumulated during earthquakes, the rigidity in the moment-rotation relationship decreases and becomes nonlinear with respect to the moment because of the gradual uplift. In addition, the moment-vertical displacement relationship must vary with the uplift. Therefore, an apparent elastic rigidity associated with the rocking-induced uplift is introduced and incorporated into a typical elasto-plastic macro element theory.

As indicated in Fig. 5, suppose the footing is loaded

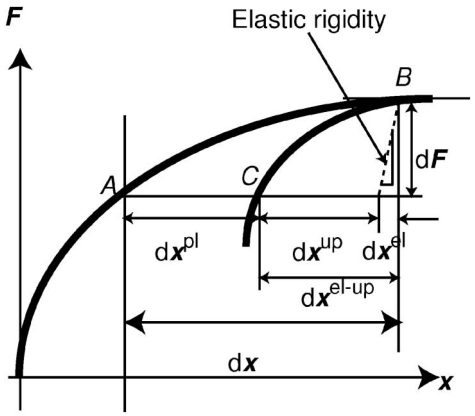

Fig. 5. Decomposition of displacement

from point A to point B with an incremental load, $\mathrm{d}\boldsymbol{F}$, each displacement component contained in the loading path A-B can be interpreted by the subsequent unloading process from point B to point C. The plastic component is the residual displacement after the unloading, $\mathrm{d}\boldsymbol{x}^{\mathrm{pl}}$. Then, except for the plastic part, the incremental displacement is no longer simply regarded as the purely elastic part, $\mathrm{d}\boldsymbol{x}^{\mathrm{el}}$, but also contains the uplift-induced component, $\mathrm{d}\boldsymbol{x}^{\mathrm{up}}$, resulting in the degradation in the apparent elastic rigidity. The incremental displacement except for the plastic part is denoted as $\mathrm{d}\boldsymbol{x}^{\mathrm{el\text{-}up}}$. Eventually, the total displacement increment, $\mathrm{d}\boldsymbol{x}$, is expressed by substituting $\mathrm{d}\boldsymbol{x}^{\mathrm{el\text{-}up}}$ into Eq. (6) instead of $\mathrm{d}\boldsymbol{x}^{\mathrm{el}}$:

$$\mathrm{d}\boldsymbol{x}=\mathrm{d}\boldsymbol{x}^{\mathrm{el\text{-}up}}+\mathrm{d}\boldsymbol{x}^{\mathrm{pl}} \tag{12}$$

When a constitutive equation for the apparent elastic component is assumed as

$$\mathrm{d}\boldsymbol{x}^{\mathrm{el\text{-}up}}=\boldsymbol{D}^{\mathrm{el\text{-}up}}\mathrm{d}\boldsymbol{F}, \tag{13}$$

the stiffness matrix of macro element, $\boldsymbol{C}$, of Eq. (11) can be rewritten as

$$\boldsymbol{C}=(\boldsymbol{D}^{\mathrm{el\text{-}up}}+\boldsymbol{D}^{\mathrm{pl}})^{-1} \tag{14}$$

This matrix is hereinafter referred to as the elasto-uplift-plastic macro element. Equation (13) is assumed to basically follow the Specifications for Highway Bridges, namely, the Beam-on-Winker foundation theory that considers the rocking-induced uplift effects, as described in the previous section. Therefore, no residual displacement is involved in the apparent elastic displacement component, whereas any residual displacement is attributed to the plastic component.

For Eq. (13), experimental findings (Shirato et al., 2008; Gajan et al., 2005; Haya and Nishimura, 1998) have indicated that the uplift makes the unloading and reloading paths of the moment-rotation and moment-vertical displacement curves depart from their monotonic backbone curves. Based on experimental results, Shirato et al. (2008) have suggested that the hysteresis rule of moment-rotation and moment-vertical displacement curves can be modeled as a peak and origin oriented rule with a function of both positive and negative maximum

moments. This matches the assumption that the apparent elastic component of rotation and vertical displacement will not leave any residual displacement at $M=0$ after unloading. Therefore, the present paper will follow such phenomenological hysteresis rules for $\theta^{\text{el-up}}$-M and $v^{\text{el-up}}$-M relationships.

The detailed formulation of Eq. (13) follows the procedure of Cremer et al. (2002) for facilitating the determination of the contribution of the uplift to the apparent elastic displacement. $d\boldsymbol{x}^{\text{el-up}}$ is decomposed into a purely elastic part, $d\boldsymbol{x}^{\text{el}}$, and an uplift-induced elastic part, $d\boldsymbol{x}^{\text{up}}$, as follows:

$$d\boldsymbol{x}^{\text{el-up}} = d\boldsymbol{x}^{\text{el}} + d\boldsymbol{x}^{\text{up}} \tag{15}$$

As indicated in Fig. 5, the purely elastic component, $d\boldsymbol{x}^{\text{el}}$, is calculated by multiplying the initial rigidity by the incremental force, $d\boldsymbol{F}$, and the uplift component, $d\boldsymbol{x}^{\text{el-up}}$, is derived by subtracting $d\boldsymbol{x}^{\text{el}}$ from the apparent elastic displacement increment, $d\boldsymbol{x}^{\text{el-up}}$. Accordingly, the compliance, $\boldsymbol{D}^{\text{el-up}}$, in Eqs. (13) and (14) is rewritten as

$$\boldsymbol{D}^{\text{el-up}} = \boldsymbol{D}^{\text{el}} + \boldsymbol{D}^{\text{up}} \tag{16}$$

and $\boldsymbol{D}^{\text{up}}$ is the compliance for the uplift displacement component.

Note that an alternative approach to consider the rocking-induced apparent elastic behavior is described in a companion paper (Paolucci et al., 2008), in which a degradation rule for the elastic rotation rigidity is proposed to take into account that an arch-like shape on the soil surface underneath the footing is formed as the cycles of rocking increase (Shirato et al., 2008; Gajan et al., 2005). The companion paper gave the degradation in the elastic rotation rigidity as a function of plastic rotation. Although the results showed that such a degradation rule noticeably improved the predicted overall response, especially the vibration frequency characteristic during the most severe excitation phases, the degradation function was determined by trial and error. The present paper will explore a general approach, setting the apparent elastic rigidity in both vertical-rocking and moment-rocking responses as a function of uplift.

PURELY ELASTIC COMPONENT

The present paper assumes the following elastic compliance:

$$D_{11}^{\text{el}} = 1/K_{\text{v}},\ D_{22}^{\text{el}} = 1/K_{\text{h}},\ D_{33}^{\text{el}} = 1/K_{\text{r}},\ \text{and (Off diagonal terms)} = 0 \tag{17}$$

K_{v}, K_{h}, and K_{r} are the equivalent elastic spring coefficients of the soil-footing system corresponding to the vertical, translational, and rocking modes of vibration, respectively. Because of the relatively smooth change of dynamic impedances with frequency, the static parts, i.e., the real parts at zero frequency, are chosen. For a square footing,

$$K_{\text{v}} = \frac{4.54G(B/2)}{1-\nu},\ K_{\text{h}} = \frac{9G(B/2)}{2-\nu},$$

$$\text{and } K_{\text{r}} = \frac{3.6G(B/2)^3}{1-\nu} \tag{18}$$

where G and ν are the shear modulus and Poisson's ratio of the underlying soil and B is the footing length (Gazetas, 1991).

APPARENT ELASTIC COMPONENT

The formulation of the apparent elastic component is based on the nonlinear moment-rotation relationship described in the Specifications for Highway Bridges (Japan Road Association, 2002) and reviewed above. In addition, the Specifications for Highway Bridges assume that, with a particular vibration mode, the vertical force is almost constant and is equal to the dead load, V_0, during an earthquake. The present paper will integrate these notions with a strain hardening macro-element theory. The reduction in the apparent elastic rigidity is taken into account in the moment-rotation (M-θ) and moment-vertical displacement (M-v) relationships. In addition, origin-oriented hysteresis rules that confirm no residual displacement at $M=0$ will be formulated based on the experimental observation (Shirato et al., 2008) for the apparent elastic components of the M-θ and M-v relationships.

Backbone Curve of Moment-Rotation Relationship

First, the rotation, θ, in Eqs. (2) and (3) is decomposed into a purely elastic component and an uplift component:

$$\theta = \theta^{\text{el-up}} = \theta^{\text{el}} + \theta^{\text{up}} \tag{19}$$

Equations (2) and (3) are rewritten as:

$$M = M_0 \times (\theta^{\text{el-up}}/\theta_0^{\text{el-up}}) \quad \text{if } M \le M_0, \tag{20}$$

$$M = M_0 \times (3 - 2\sqrt{\theta_0^{\text{el-up}}/\theta^{\text{el-up}}}) \quad \text{if } M > M_0 \tag{21}$$

where M_0 and $\theta_0^{\text{el-up}}$ are the moment and apparent elastic rotation angle at which the uplift initiates and an edge of the footing starts to separate from the underlying soil.

The mobilized moment should be smaller when the underlying soil becomes plastic than when it is assumed to remain elastic. Therefore, the moment, M, in Eqs. (20) and (21), is rewritten using the following procedure. Calculate a critical moment, M_{cr}, by substituting $H=0$ and $V=V_0$ into Eq. (4) and another critical moment, M_∞, by taking $\theta^{\text{el-up}} \to \infty$ in Eq. (21). Take the ratio of these two moments as:

$$\alpha = M_{\text{cr}}/M_\infty \tag{22}$$

where $M_\infty = 3M_0$. α is a reduction factor in the moment and is applied to the terms of M_0 in Eqs. (20) and (21).

$$M = M_\alpha \times (\theta^{\text{el-up}}/\theta_0^{\text{el-up}}) \quad \text{if } M \le M_\alpha, \tag{23}$$

$$M = M_\alpha \times (3 - 2\sqrt{\theta_0^{\text{el-up}}/\theta^{\text{el-up}}}) \quad \text{if } M > M_\alpha \tag{24}$$

where the moment and rotation at which the uplift initiates are redefined as:

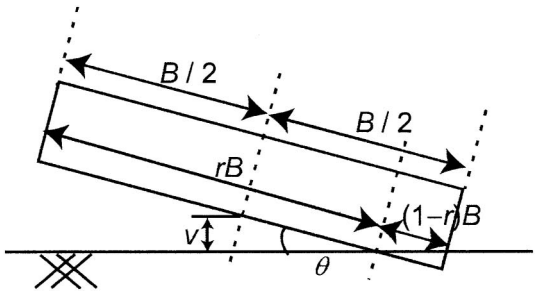

Fig. 6. Geometrical relationship between rotation θ and vertical displacement v at the base center of the footing while the footing is uplifted by the moment due to the positive rotation of θ

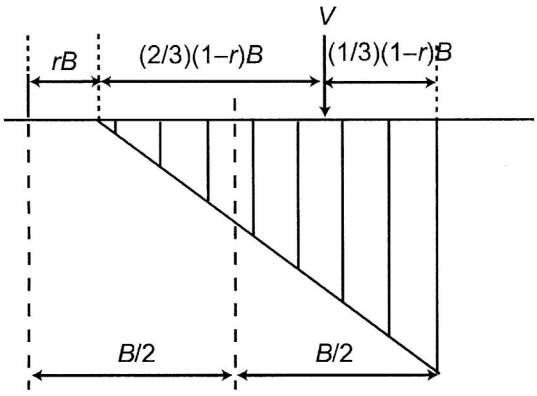

Fig. 7. Soil reaction stress distribution at the base of the footing from an underlying elastic medium

$$M_\alpha = \alpha M_0 = \alpha B V_0/6, \quad \theta_0^{\text{el-up}} = M_\alpha / K_r \tag{25}$$

For simplicity, the crude assumption that $H=0$ is used in the estimation of M_{cr} and this assumption should be confirmed via future numerical calibration processes. Note that, if α becomes larger than 1 in Eq. (22), it should be replaced with 1, because it indicates that uplift is the dominant factor in the nonlinearity of footing-soil interaction.

Then, Eqs. (23) and (24) are solved in terms of $\theta^{\text{el-up}}$ and the purely elastic component, θ^{el}, is subtracted from $\theta^{\text{el-up}}$. Finally, the θ^{up}-M relationship is derived as follows:

$$\theta^{\text{up}} = 0 \quad \text{if } M \le M_\alpha, \tag{26}$$

$$\theta^{\text{up}} = \left\{ \frac{4}{(3 - M/M_\alpha)^2} - \frac{M}{M_\alpha} \right\} \theta_0 \quad \text{if } M > M_\alpha \tag{27}$$

Backbone Curve of the v^{up}-M Relationship

When the footing is partially uplifted, the geometry of the footing is modeled as shown in Fig. 6. The length of the uplifted area of footing is defined as rB and that of the contact area that meets the underlying soil is derived as $r(1-B)$. r can be derived as a function of the moment M. Figure 7 shows the soil reaction stresses when one part of the footing is uplifted, while the other part meets the underlying soil. First, for simplicity, the underlying soil is assumed to be elastic, resulting in the soil resistance stress being distributed in a triangular shape. As shown in Fig. 7, since the subgrade reaction stress distribution has a triangular shape, the moment, M, at the base center of the footing is derived as:

$$M = V\left(\frac{B}{2} - \frac{(1-r)B}{3} \right) \tag{28}$$

Substituting the first equation of Eq. (1) into BV of Eq. (28) yields the following equation:

$$r = \frac{1}{2}\left(\frac{M}{M_0} - 1 \right) \tag{29}$$

Then, r is redefined as follows, by replacing M_0 with M_α in Eq. (29),

$$r = \frac{1}{2}\left(\frac{M}{M_\alpha} - 1 \right) \tag{30}$$

Based on the geometry shown in Fig. 6, the vertical displacement at the base center of the footing, v, is obtained as

$$v = -\left(rB - \frac{B}{2} \right)\theta \tag{31}$$

where the vertical displacement, v, is positive while the center of the footing is in contact with the underlying soil. v and θ are equivalent to $v^{\text{el-up}}$ and $\theta^{\text{el-up}}$, respectively. Accordingly, Eq. (31) is rewritten as:

$$v^{\text{el-up}} = -\left(rB - \frac{B}{2} \right)\theta^{\text{el-up}} \tag{32}$$

The uplift component in the vertical displacement, v^{up}, is obtained by subtracting v_0 from $v^{\text{el-up}}$, where v_0 is the vertical displacement at the time when the footing starts to partially uplift and the edge of the footing starts to separate from the underlying soil:

$$v^{\text{up}} = \left(\frac{B}{2} - rB \right)\theta^{\text{el-up}} - v_0 \tag{33}$$

$$v_0 = \frac{B}{2}\theta_0^{\text{el-up}} \tag{34}$$

Finally, the v^{up}-M relationship after the footing starts to partially uplift can be derived using Eqs. (24), (30), (33), and (34) as follows:

$$v^{\text{up}} = 0 \quad \text{if } M \le M_\alpha, \tag{35}$$

$$v^{\text{up}} = -\frac{B}{2}\left\{ \frac{4}{\left(3 - \frac{M}{M_\alpha}\right)^2} - \frac{4}{\left(3 - \frac{M}{M_\alpha}\right)} + 1 \right\} \quad \text{if } M > M_\alpha, \tag{36}$$

Equation (35) indicates that v^{up} equals zero until the moment, M, reaches the uplift threshold moment, M_α.

Phenomenological Hysteresis Rules for θ^{up}-M and v^{up}-M Relationships

As noted above, Shirato et al. (2008) experimentally observed that the hysteresis rules of moment-rotation and moment-vertical displacement curves can be modeled as a peak and origin oriented rule with a function of both positive and negative maximum moments. Figure 8 illus-

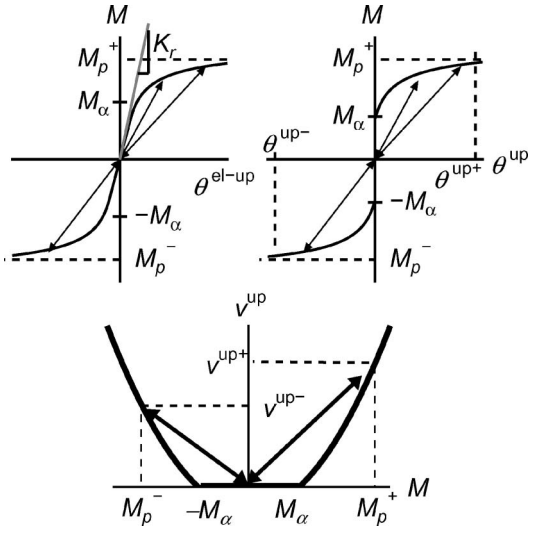

Fig. 8. Hysteresis behavior of the uplift components due to rotation and vertical displacement, θ^{up} and v^{up}, due to moment M

trates the hysteresis rule proposed in the present paper. M_p^- and M_p^+ are the largest moments on the negative and positive sides, respectively, until time $t=t$. The corresponding rotations are defined as θ^{up-} and θ^{up+}, respectively, and the corresponding vertical displacements are defined as v^{up-} and v^{up+}, respectively. The unloading or reloading path follows a straight line connecting the largest moment points on the monotonic loading curve to the origin.

$$\theta^{up}=\frac{\theta^{up-}}{M_p^-}M \quad \text{if } M<0 \qquad \theta^{up}=\frac{\theta^{up+}}{M_p^+}M \quad \text{if } M>0 \tag{37}$$

$$v^{up}=\frac{v^{up-}}{M_p^-}M \quad \text{if } M<0 \qquad v^{up}=\frac{v^{up+}}{M_p^+}M \quad \text{if } M>0 \tag{38}$$

For the θ^{up}-M and v^{up}-M relationships, the term 'unloading' refers to the case in which the increment of moment $|M|$ is negative, and the term reloading denotes a path that moves towards the previous unloading point on the monotonic loading curve, followed by unloading. When a reloading path reaches the point M_p^- or the point M_p^+ on the monotonic loading curve and the absolute value of the moment continues to increase, the path follows the monotonic loading curve.

Incremental Apparent Elastic Compliance

Finally, the uplift compliance, $\boldsymbol{D}^{up}$, can be obtained by differentiating the above hysteresis rules in terms of moment M. In addition, a mode shift is taken into account, as proposed by Cremer et al. (2002). The plastic deformation of the soil is considered to become predominant in the total deformation as the dead load increases, while the uplift component becomes predominant as the dead load decreases. Accordingly, a weight function of $(1-V_0/V_m)$ will be applied to the compliance, where V_0 is the dead load and V_m is the ultimate bearing capacity for the centered vertical loading. Finally, the uplift compliance, $\boldsymbol{D}^{up}$, can be expressed as follows:

$$D_{13}^{up}=\left(1-\frac{V_0}{V_m}\right)\times\left(\frac{\partial v^{up}}{\partial M}\right), \tag{39}$$

$$D_{33}^{up}=\left(1-\frac{V_0}{V_m}\right)\times\left(\frac{\partial \theta^{up}}{\partial M}\right), \tag{40}$$

$$(\text{Others})=0 \tag{41}$$

Uplift will not occur when $V_0/V_m=1$.

Finally, an apparent elastic compliance considering uplift, $\boldsymbol{D}^{el\text{-}up}$, is obtained via Eq. (16) as:

$$\boldsymbol{D}^{el\text{-}up}=\begin{pmatrix} D_{11}^{el} & 0 & D_{13}^{up} \\ 0 & D_{22}^{el} & 0 \\ 0 & 0 & D_{33}^{el}+D_{33}^{up} \end{pmatrix} \tag{42}$$

Note that, as a numerical technique, the points (M_p^-, θ^{up-}) and (M_p^+, θ^{up+}) on the monotonic θ^{up}-M curve should be calculated based on the history of the accumulated value of $d\theta^{up}$, where $d\theta^{up}$ is calculated with $d\theta^{up}=\boldsymbol{D}^{up}\,d\boldsymbol{F}$ once the moment exceeds the threshold uplift moment, M_α. The same method is also used for the v^{up}-M relationship. This method is used in order to avoid difficulty in calculating accuracy. As shown in Fig. 8, in the backbone curve of the θ^{up}-M relationship, $dM/d\theta^{up}$ approaches zero as M increases. This means that a minor numerical error in moment, M, can cause a large variation in rotation θ^{up}, as the moment increases, and the error in the unloading-reloading gradients of θ^{up-}/M_p^- and θ^{up+}/M_p^+ may become significant.

PLASTIC COMPONENT

The Nova and Montrasio model (1991) is used to describe plastic deformations. The yield function, f_y, is defined as follows:

$$f_y=h^2+m^2-\xi^2(1-\xi/\rho_c)^{2\zeta}=0 \tag{43}$$

where ρ_c is the hidden parameter that specifies the instantaneous size of the yield surface and translates the instantaneous combined loads into the norm of an equivalent vertical force. ρ_c is obtained by substituting the instantaneous combined loads, V, H, and M, into Eq. (44) of the Nova-Montrasio paper (Nova and Montrasio, 1991) shown below:

$$\rho_c=\frac{\xi}{1-\left(\dfrac{h^2+m^2}{\xi^2}\right)^{1/(2\xi)}} \tag{44}$$

When ρ_c evolves and finally reaches 1, the yield surface coincides with the bearing capacity surface, f_{cr}, defined in Eq. (4). After that, the yield surface will not evolve or penetrate the bearing capacity surface for any loading. When a combined load point, $\boldsymbol{F}(t)$, is located on the surface of Eq. (43) in the V-H-M/B space at time $t=t$ and an incremental combined load vector, $d\boldsymbol{F}(t)$, is directed outward, the surface expands during the subsequent time step so that $\boldsymbol{F}(t+dt)=\boldsymbol{F}(t)+d\boldsymbol{F}(t)$ can be included on the renewed surface of Eq. (43) again.

A non-associated flow rule is adopted.

$$d\boldsymbol{x}^{pl} = \Lambda \frac{\partial g}{\partial \boldsymbol{F}} \tag{45}$$

where Λ is a scalar parameter and g is the plastic potential function defined as follows:

$$g = \lambda^2 h^2 + \chi^2 m^2 - \xi^2 (1 - \xi/\rho_g)^{2\zeta} = 0 \tag{46}$$

where $\lambda = \mu/\mu_g < 1$, $\chi = \phi/\phi_g < 1$, and μ_g and ϕ_g are the parameters that specify the shape of the plastic potential surface in the *V-H-M/B* space.

The hardening function is given based on the response of a footing to centered vertical loading. The relationship between vertical force, V, and vertical displacement of the plastic component, v^{pl}, can be approximated with an exponential function (Nova and Montrasio, 1991; Gottardi and Butterfield, 1995).

$$\frac{V}{V_m} = 1 - \exp\left(-\frac{R_0 v^{pl}}{V_m}\right) \tag{47}$$

where R_0 is the initial gradient of the V-v^{pl} curve. To apply Eq. (47) to combined loading, the term, V/V_m, in the left-hand side is replaced by the size of the yield surface, ρ_c, of Eq. (44), and v^{pl} in the right-hand side is replaced with x_c, the geometric mean of plastic components of v, u, and θ, that is defined by the following equation:

$$x_c = \{(v^{pl})^2 + (\alpha_M u^{pl})^2 + (\gamma_M B \theta^{pl})^2\}^{0.5} \tag{48}$$

where α_M and γ_M are the non-dimensional parameters that incorporate the contribution of horizontal displacement and rotation into hardening. Eventually, the hardening function for combined loading can be obtained as:

$$\rho_c = 1 - \exp\left(-\frac{R_0 x_c}{V_m}\right) \tag{49}$$

Since the compliance is formulated in a rate form in this paper, a rate-form of the hardening function is estimated, using the Taylor expansion and taking the first-order terms.

$$d\rho_c = (1 - \rho_c)\frac{R_0}{V_m}(|dv^{pl}| + \alpha_M |du^{pl}| + \gamma_M B |d\theta^{pl}|) \tag{50}$$

Finally, the plastic compliance is obtained as follows:

$$\boldsymbol{D}^{pl} = \frac{1}{K}\frac{\partial g}{\partial \boldsymbol{F}}\frac{\partial f_y}{\partial \boldsymbol{F}^T} \tag{51}$$

where K is the hardening coefficient and is defined as:

$$K = -\frac{\partial f_y}{\partial V_c}\frac{\partial V_c}{\partial (\boldsymbol{x}^{pl})^T}\frac{\partial g}{\partial \boldsymbol{F}} \tag{52}$$

In addition, the compliance for the condition of $H = M = 0$ is separately calculated, because the yield surface and the plastic potential surface in the *V-H-M/B* space have an apex on the V-axis. The compliance for the case of $H = M = 0$ is given as the inverse of the tangent gradient of Eq. (47):

$$D_{11}^{pl}(t) = 1/(1 - \rho_c)/R_0, \quad (\text{Others}) = 0 \tag{53}$$

Finally, when the apparent elastic behavior due to uplift is taken into account, V is fixed as the dead load, V_0, during earthquakes or eccentric loading processes to agree with the assumption in the formulation of the apparent elastic constitutive equation.

Plastic deformation occurs when an instantaneous incremental load moves along the perimeter of the current yield surface or moves outward from the current yield surface. However, when an instantaneous load increment lies inside the current yield surface, no plastic compliance is included in the incremental compliance given by Eq. (9) or (14), and the footing responds elastically or apparent-elastically.

NUMERICAL TECHNIQUES

The present study deals with superstructure-single pier-footing-soil systems. The mass and rotation inertia of the superstructure are modeled with a lumped mass. The pier is assumed to respond linearly and is modeled with Bernoulli-Euler beam elements. The P-Delta effect is considered with a geometric stiffness matrix of the beam-column theory, and the axial force in the geometric matrix will not change from the initial state during a numerical simulation. Accordingly, an element stiffness matrix for the pier is expressed as the superposition of the Bernoulli-Euler beam element matrix and the geometric stiffness matrix. An element lumped mass matrix is also assigned to each pier beam element. The footing is also modeled with a lumped mass, taking the mass and rotation inertia into account. The soil-footing interaction is modeled with the macro element.

In static analyses, a simple incremental calculation is conducted without any iteration process. For dynamic analyses, the equation of motion is given as follows:

$$\boldsymbol{M}\ddot{\boldsymbol{x}}(t) + \boldsymbol{H}\dot{\boldsymbol{x}}(t) + \boldsymbol{K}^S\boldsymbol{x}(t) + \boldsymbol{F}(t) = \boldsymbol{p}(t) \tag{54}$$

where $\boldsymbol{M}$ is the mass matrix, $\boldsymbol{H}$ is the damping matrix, $\boldsymbol{K}^S$ is the stiffness matrix for the pier, $\boldsymbol{F}$ is the soil reaction force matrix from the macro element, and $\boldsymbol{p}$ is the external force matrix. The Newmark-β scheme is used for the integration with regard to time. The soil resistance forces are functions of the loads, and strictly speaking, they continue to change during a time step from $t = t$ to $t = t + dt$. However, the macro-element is formulated in a rate form. Therefore, for simplicity, the soil reaction forces are solved explicitly. The soil reaction forces and displacements of the macro element at $t = t + dt$ are obtained as:

$$\boldsymbol{F}(t + dt) = \boldsymbol{F}(t) + d\boldsymbol{F}(t) = \boldsymbol{F}(t) + \boldsymbol{C}(t)(x(t + dt) - x(t)) \tag{55}$$

where $\boldsymbol{C}$ is calculated with Eq. (11) or (14). The stiffness matrix of the macro element is set using the load at $t = t$, $\boldsymbol{F}(t)$, and it is assumed to be unchanged during the time step from $t = t$ to $t = t + dt$. Instead of accepting these approximations, an incremental time step, dt, was taken to be sufficiently small. The common values of parameters, γ and β, in the Newmark-β method are set as 0.5 and 0.25, respectively.

To calculate the plastic components of displacement, the following method is adopted in order to judge

whether the loading condition is satisfied during the generic time step. First, a trial calculation from $t = t$ to $t = t + dt$ is executed with the apparent elastic stiffness matrix employed in the previous time step, and an incremental load, $dF(t)$, is obtained. The summation of $F(t) + dF(t)$ is substituted into Eq. (44), and the temporary size of the yield surface, $\rho_c(t + dt)$, is calculated. If the temporary size of the yield surface, $\rho_c(t + dt)$, is smaller than $\rho_c(t)$, then it is specified that the macro element responds within the yield surface during the time step, i.e., the macro element responds in an elastic or apparently elastic manner. If the temporary size of the yield surface, $\rho_c(t + dt)$, is larger than $\rho_c(t)$, then, as assumed, the macro element responds elasto-plastically. If necessary, the uplift compliance is also redefined. When the trial calculation above gives a smaller negative moment or a larger positive moment than the macro element has experienced, M_p^- or M_p^+, the θ^{up}-M and uplift-related v^{up}-M relationships follow their backbone curves. Finally, the recalculation starts over for the current time step considering the redefined compliances based on the preceding trial calculation result.

When the plastic deformation of the macro element is considered in a time step from $t = t$ to $t = t + dt$, the value of ρ_c in Eq. (43) is also updated at $t = t + dt$. M_p^-, M_p^+, θ^{up-}, and θ^{up+} are renewed if necessary. Note that, if the temporal value of $\rho_c(t + dt)$ numerically becomes larger than 1, then $\rho_c(t + dt)$ is set to be 1, because, theoretically, ρ_c cannot exceed 1.

MODEL EXPERIMENTS OF PIER FOOTING SYSTEMS

Two types of model experiments of pier-footing systems on dry sand will be simulated: model pier-footing systems subjected to monotonic lateral loading on the top of the pier and a model pier-footing systems subjected to shake table loading. Detailed results for both experiments are examined in a companion paper (Shirato et al., 2008), and the in-depth experimental reports are available as Technical Memorandums of Public Works Research Institute, Nos. 4027 and 4028 (2007) with CD-ROMs that include measured raw data.

Monotonic Lateral Loading Experiment

The experiments were conducted at the Foundation Engineering Laboratory in the Public Works Research Institute, Tsukuba, Japan.

Figure 9 shows a schematic diagram and a photograph of the model setup. In a deep test pit of 4 m in length and 4 m in width, a dry Toyoura sand deposit having a thickness of 2 m and an average relative soil density of $D_r = 80\%$ (soil density $\rho = 1.60 \times 10^3$ kg/m^3) was made. The deposit was compacted in layers so that homogeneous soil conditions were achieved. CD triaxial compression tests revealed that the internal friction angle $\phi = 42.1°$ at $D_r = 80\%$.

Figure 10 shows a schematic diagram of the model pier footings. A model pier footing was located on the center

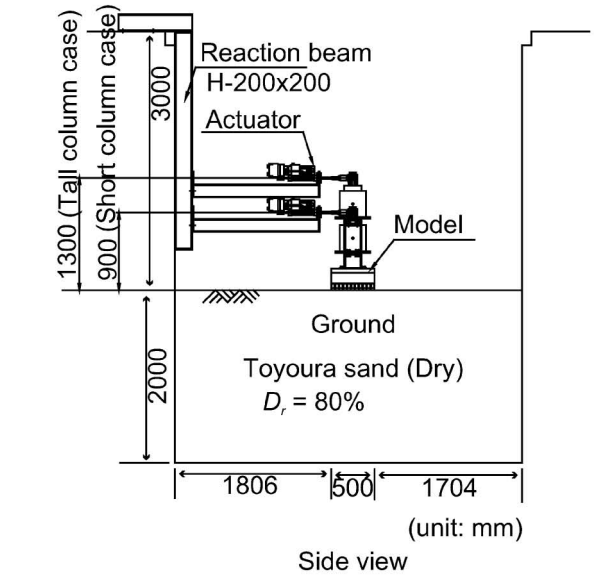

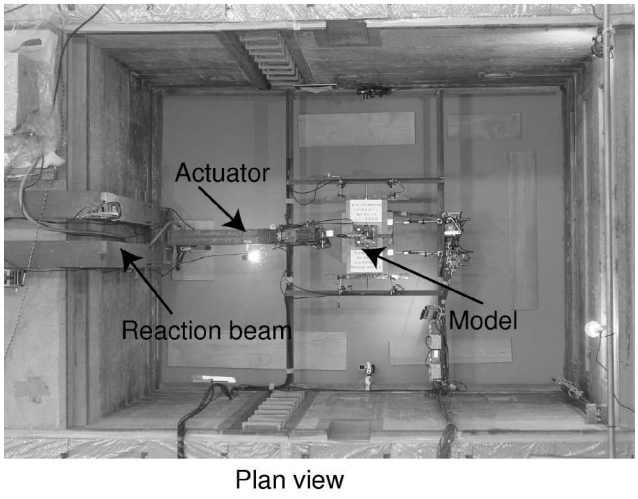

Fig. 9. Model set-up of the monotonic loading experiment

of the sand deposit surface. The models comprise of three structural components: a top steel rack, a steel I-beam column, and a footing. Every structural component was stiff enough to consider the model to be rigid, and the structural components were rigidly connected to each other. The footing shape was a 0.5 m square block of 0.25 m in depth. Eleven bi-directional load cells were attached at the base of the footing along the loaded direction, so that the distribution of normal and shear reactions to the base of the footing was captured. The long side of the load cell had the same length as the foundation side and the short side of the load cell was in the loaded direction. Sandpaper was attached at the contact surface where the load cells met the soil, so that the boundary condition was rough. The universal joint was attached to the model pier footing to connect the footing to the actuator system. At the universal joint, the model was free to rotate and move up and down.

The combined slow monotonic V-H-M loadings with a dead load, V_0, i.e., the dead weight of the model pier

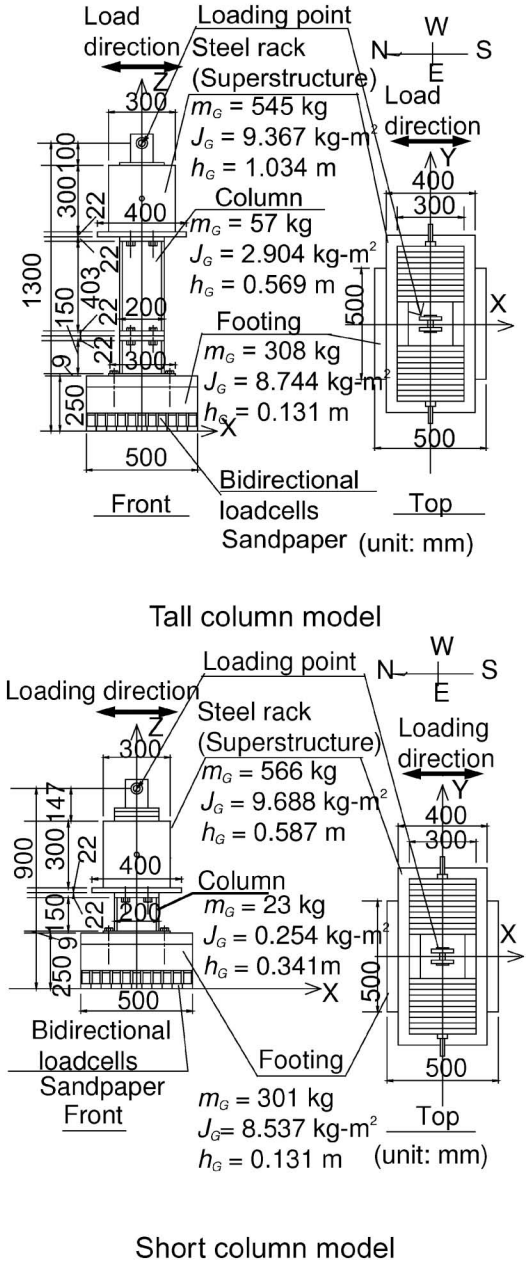

Fig. 10. Schematic diagram of pier-footing models in the monotonic loading experiment

footing, were achieved by gradually applying a horizontal North-South displacement at a fixed height via a computer-controlled servo actuator. During the loading phase, displacement was controlled and increased up to the nominal jack stroke capacity (10 mm), and the load was then released to zero during the unloading phase. The behavior for different *V-H-M* combinations was examined at various heights of the loading point and the soil densities. The height of the loading point was varied using two columns of different heights but the same I cross-section. These columns are referred to as short and tall columns. The non-dimensional ratios of applied moment, M, to horizontal force, H, at the base center point of the footing, $M/H/(B/2)$, were 3.6 and 5.2 for the short and tall columns, respectively.

Table 1. Simulated cases of monotonic loading experiment

Cases	Soil relative density D_r	Column
80T	80%	Tall
80S	80%	Short

Figure 10 also shows the mass, m_G, the structural moment of inertia about the center of gravity, J_G, and the height from the footing base to the center of gravity, h_G, for each structural component. The model pier footings have mechanical properties similar to those of typical highway bridge pier footings in terms of the value of h_G/B and the static safety factors (Shirato et al., 2008). The initial safety factor was 28, where the bearing capacity was estimated via the centered vertical loading experiment described below.

The cases for the simulation with regard to the monotonic loading experiment are listed in Table 1. The first two digits in the case numbers indicate soil relative density, and the final letter indicates the column type.

Shake Table Experiment

Shake table experiments were conducted at the Large-scale Shake Table Facility at the Public Works Research Institute, Tsukuba, Japan. Figures 11 and 12 show the model set-up. For the simulation below, two cases are chosen from all of the excitation cases in the experiment, and they are listed in Table 2.

The size of the shake table was 8 m × 8 m, as viewed from above. The shake table was rocked in the North-South direction, and the positive direction of X in Fig. 11 and the North direction in Fig. 12 were coincident. Two different types of seismic acceleration records that were observed on sturdy ground were input to the shake table. The input wave forms are shown in Fig. 13. Since the mass of the shake table and the soil deposit was huge, the earthquake motions were not perfectly reproduced by the shake table. Accordingly, both the original records and the measured motions on the shake table were plotted in Fig. 13. The Type I motion represents interplate-type earthquakes and contains a much larger number of cycles than the Type II motion, while the Type II motion represents inland-strike-type earthquakes. The Type I motion used in the experiment was recorded during the 1993 Kushiro-Oki earthquake in Japan. The Type II motion used in the experiment was recorded during the 1995 Kobe earthquake in Japan, while a 20% reduction in the acceleration of the second wave form was applied to avoid excessive earthquake loading to complete the observation of the nonlinear behavior of the model. The horizontal motions at the ground surface are shown in Fig. 14 along with their acceleration response spectrum (ARS) curves at a damping factor of 5%.

A laminar shear box of 4 m internal length, 4 m internal width, and 2.1 m internal depth was placed on the shake table. The box is comprised of 10 layered frames. The dry Toyoura sand deposit used in the monotonic loading experiment was also used in this experiment. The

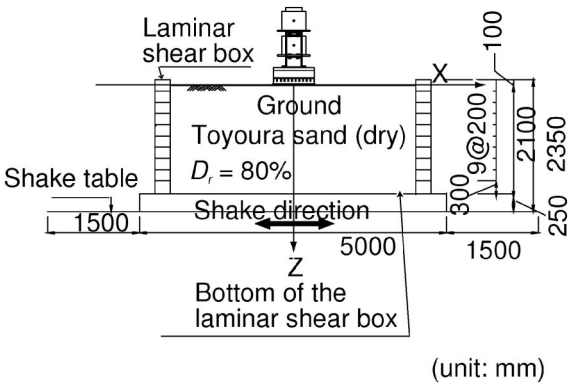

Fig. 11. Model set-up of shaking table experiment

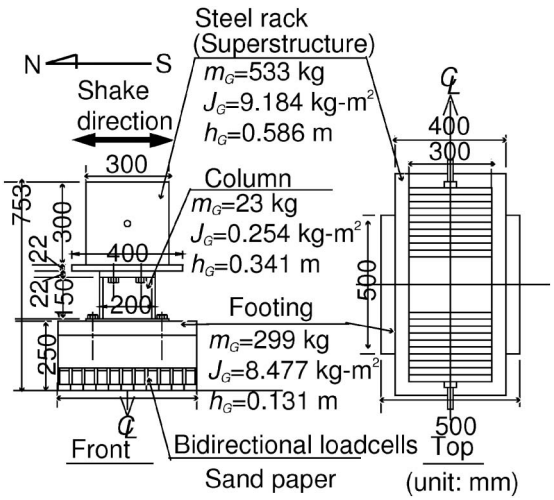

Fig. 12. Schematic diagram of pier-footing model in the shaking table experiment

Table 2. Simulated cases of shake table experiment

Case	Earthquake Type	Maximum acceleration on the table (Gal)
Case 1	Type I	601
Case 2	Type II	557

sand deposit was constructed up to a height of 2 m in the laminar shear box and was compacted in layers so that a satisfactory homogeneous soil condition was obtained. The soil relative density, D_r, of 80% was also the same.

Basically, the model pier footing was the same as that used in the monotonic loading experiment, while only the short column model was used. Since the universal joint was removed, the mass of the model pier footing was slightly different from that in the monotonic loading experiment. Figure 12 also shows the mass, the moment of inertia, and the height of the center of gravity from the footing base in terms of each structural component: a steel rack, an I-beam column, and a footing.

The model pier footing was placed at the center of the soil surface. Some test runs were performed separately

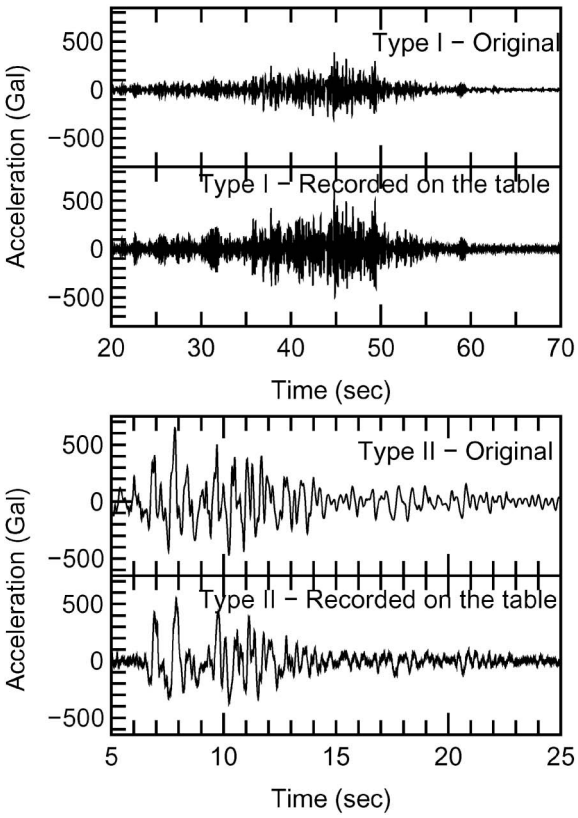

Fig. 13. Earthquake waves input onto the shaking table: Type I wave = 1993 Kushiro-oki Earthquake record, Type II wave = 1995 Kobe Earthquake record

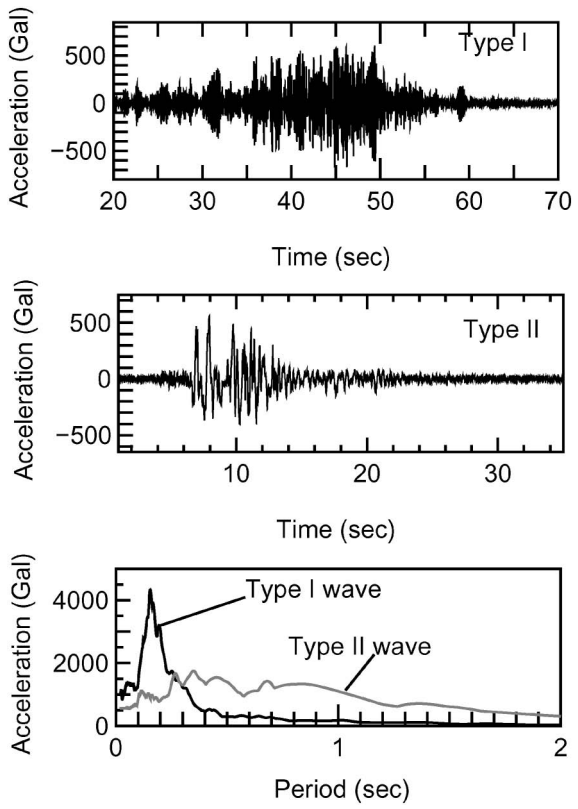

Fig. 14. Base input accelerations to the footing (or horizontal acceleration at ground level) and their ARS curves

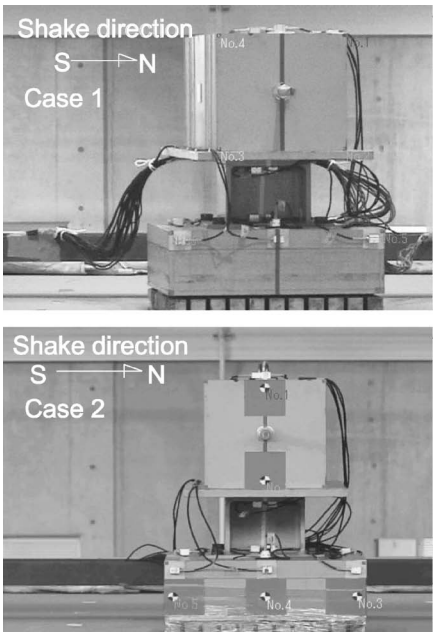

Fig. 15. States of the model pier footing at the excitation ends

from the experiments of the present paper, and these tests revealed that the original Kobe motion (Type II motion) was too strong to observe the foundation response until the end of the excitation. Therefore, for Case 2, in addition to the reduction in acceleration, a 10-mm embedment (4% of the footing depth and 2% of the footing length) was added as a failsafe to prevent the toppling of the model pier footing, while it is thought that the embedment effect on the overall footing response can be disregarded.

Figure 15 shows the states of the model pier footing at the end of the excitations. The model pier footing was not toppled in either case, although irreversible displacement did occur.

PARAMETER SETTING FOR THE MACRO ELEMENT

Numerical parameters for the macro element are estimated below. Table 3 shows lists of the associated parameters. The parameters can basically be estimated via soil investigation, such as in-situ plate loading tests and soil element tests. However, the present study took advantage of the results of a centered vertical push test for the footing.

The vertical push test was conducted in the test pit at the Foundation Engineering Laboratory, as in the monotonic lateral loading experiment. The soil condition was the same as that used in the monotonic lateral loading experiment and shake table experiment. A stiff steel box filled with concrete and having a square base of 0.5 m was used as footing and was placed at the center of the soil surface. The stiff box dimension, as viewed from above, was the same as that used in the monotonic loading and shake table experiments. The entire footing base was covered with pieces of the sandpaper described above. A

Table 3. Parameters for macro element

Elastic parameters	K_v (kN/m)	89179
	K_h (kN/m)	72794
	K_r (kN·m/rad)	4420
Hardening parameters	R_0 (kN/m)	48946
	V_m (kN)	244.8
	α_M	2.8
	γ_M	1.7
Yield function	ζ	0.95
	μ	0.9
	ψ	0.48
Plastic potential	λ	0.45
	χ	0.45

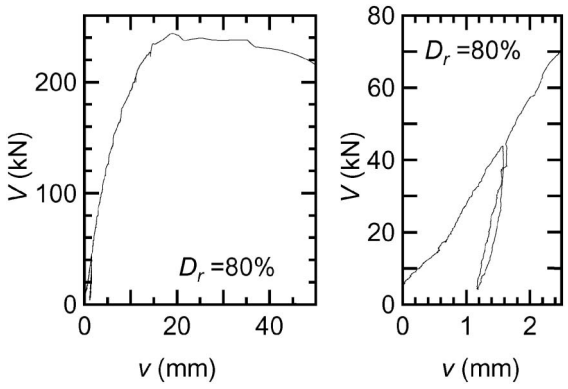

Fig. 16. Observed vertical load-settlement (V-v) curves in the centered vertical push test (left: experimental result, right: enlarged view of a part including the unloading-reloading process)

manually operated hydraulic jack was used. At an early stage of loading, a partial unloading and reloading was applied to estimate the elastic (unloading) rigidity of the soil.

Vertical, horizontal, and rotational elastic springs, K_v, K_h, and K_r, are given based on the unloading gradient observed in the centered vertical push test. The observed vertical load-settlement curve is shown in Fig. 16. The value of K_v is approximated as a gradient of the unloading path via a typical least-mean square method, as delineated in Fig. 17. The shear modulus can be derived from the first equation of Eq. (18), assuming Poisson's ratio, ν, to be 0.3, and the shear modulus is used to estimate the values of the translational and rotational springs, K_h and K_r, with the second and third equations of Eq. (18).

The essential parameters to set the evolution of the yield locus, V_m and R_0, are also deduced from the centered vertical push test result. The maximum load is given as the ultimate bearing capacity, V_m. A V-v^{pl} curve is estimated based on the measured V-v curve. v^{pl} can be derived by subtracting a calculated elastic component, $v^{el} = V/K_v$, from the corresponding vertical displacement at every loading step. Then, the V-v^{pl} curve is fit with Eq. (47). Figure 18 shows the experimental V-v^{pl} curve (solid line) and fitted curve (dashed line).

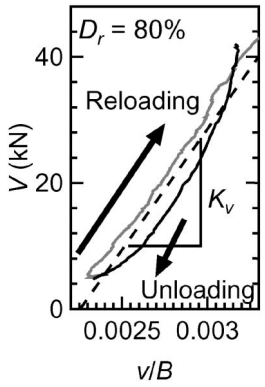

Fig. 17. Least mean square approximation as a function of unloading gradient, K_v

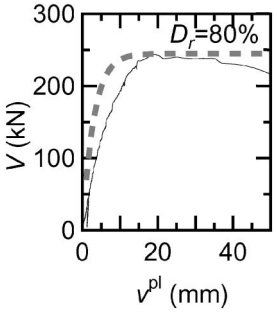

Fig. 18. Observed and fitted V-v^{pl} curves for centered vertical push test; solid line: observed curve, dash line: fitted curve

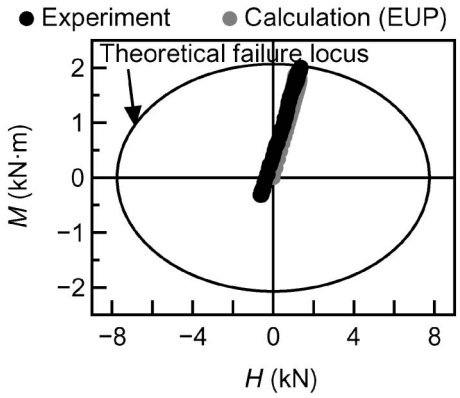

Fig. 19. Projection of measured and calculated forces and theoretical failure locus in H-M plane; Case 80T

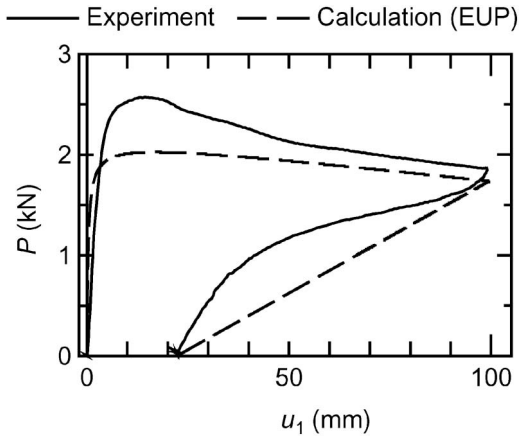

Fig. 20. Observed and calculated horizontal load-displacement (P-u_1) curves at the loading point; Case 80S

Other parameter values are selected following the typical values that have been suggested by Nova and Montrasio (1991) and Montrasio and Nova (1997) based on theoretical considerations and some experimental facts.

SIMULATION OF MONOTONIC LOADING EXPERIMENT

The initial conditions in the numerical simulation are $V = V_0$, $H = 0$, $M = 0$, and $\rho_c = V_0/V_m$, and the corresponding initial settlement of the macro-element is calculated preliminarily. The initial settlement of the macro element is also applied to all beam element nodes. In the numerical simulation, the displacement at the loading point is increased to the maximum displacement of the experiment and is then decreased. Figure 19 plots the trajectory of the observed and calculated forces in the H-M plane for Case 80T and the projection of the bearing capacity locus, Eq. (4), in which $V = V_0$, i.e., the weight of the model pier footing, and the parameters used in the simulation are taken into account. In both experiment and calculation, the soil-footing system reaches the ultimate loads, and a similar result is obtained for Case 80S.

Figure 20 shows the observed and calculated horizontal loads, P, and the horizontal displacements, u_1, for Caser 80S, where the calculation is conducted with the elasto-uplift-plastic (EUP) macro element. The calculated hysteresis loop shape agrees very well with the experimental results. While the short column was involved, the post-peak behavior in the load P is caused by the P-Delta effect. Although the calculation slightly underestimates the load, the parameter values used in the present study seem to work effectively. Therefore, the calculated results suggest that the theoretical and empirical parameter values calibrated in the past should be widely applicable.

Figure 21 shows the observed and calculated hysteresis curves of moment-settlement (M-v), moment-rotation (M-θ), and horizontal force-horizontal displacement (H-u) with the elasto-plastic (EP) macro element and the elasto-uplift-plastic (EUP) macro element (both experimental cases). In Fig. 21, settlement is positive and downward and uplift is negative and upward. The hysteresis curves calculated with the EUP macro element agree with the experimental curves. In terms of moment-settlement (M-v) curves, both the EP and the EUP macro elements take the accumulation of irreversible settlement at $M = 0$ into account. However, the M-v curves obtained with the EP macro element remain under the $v = 0$ axis. On the other hand, the EUP macro element predicts the threshold moment values at which the vertical displacement becomes negative (i.e., the base center of the footing was uplifted) very well, approximately 1.6–1.8 kN·m for the calculation and 1.4–1.8 kN·m for the experiment. Namely, the EUP macro element is capable of accounting for both the rocking-induced settlement and the uplift-induced horn-shaped hysteresis loop in the moment-settlement curve. In terms of the moment-rotation (M-θ) curves, the observed and calculated upper limits of the moment agree very well. The unloading gradients calculated with the EP macro element are much larger than those calculated with the EUP macro element and observed in the experiment. Therefore, it is confirmed that the introduction of the uplift considerably improves the numerical results, both in terms of foundation stiffness

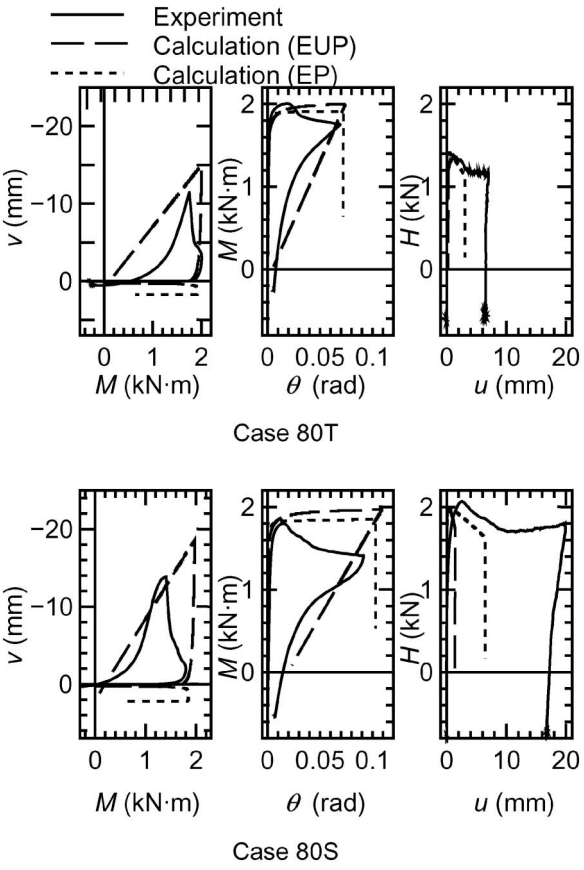

Fig. 21. Observed and calculated hysteresis curves at the base center of the footing for monotonic loading experiments

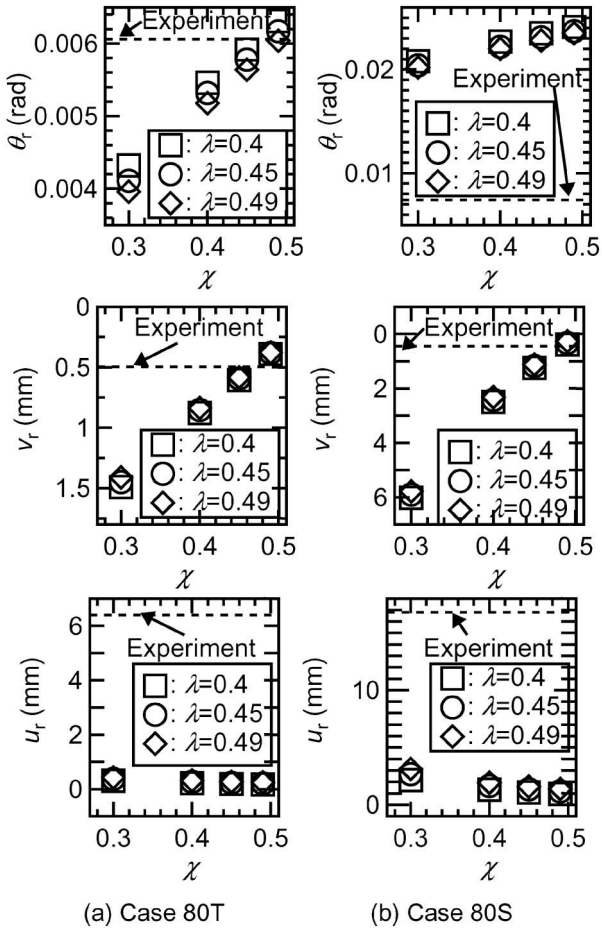

Fig. 22. Influence of the difference in the plastic potential parameters, λ and χ, on the variation in the calculated residual vertical displacement v, horizontal displacement u, and rotation θ at the base center of the footing at $P=0$ after unloading (EUP macro element)

and the shape of the hysteresis loops. In terms of horizontal force-horizontal displacement (H-u) curves, the calculation predicts the tendency that the sliding displacement abruptly increased when the horizontal load reached the upper limit value. For both the experiment and the calculation, the sliding of the footing is much smaller compared to the peak horizontal displacement at the loading point, u_1. (*See* the peak horizontal displacement at the loading point, u_1, for Case 80S in Fig. 20.) This confirms that the rocking is the prevailing response mode of the model pier footing.

Figure 22 compares the calculated residual settlements, horizontal displacements, and rotations, at the base center of the footing, v_r, u_r, and θ_r, after the load of the loading point is unloaded to zero. The experimental results are indicated by the dotted lines in Fig. 22. The calculation uses the EUP macro element considering the different values of the plastic potential parameters, λ and χ, in which Nova and Montrasio (1991) have suggested that the ranges of the values of λ and χ are smaller than 0.5. As confirmed in Fig. 22, the parameter χ is crucial because the rocking is significant in the present study. A value of 0.4–0.5 seems appropriate for χ. The calculated residual horizontal displacements are not sensitive to the difference in the parameters of λ and χ, indicating that a parameter of μ that specifies the shapes of the yield and bearing capacity surface of the macro element in terms of irreversible sliding resistance may be smaller than that considered in the present calculation.

SIMULATION OF THE SHAKE TABLE EXPERIMENT

This section will examine the capability of the macro element for estimating the dynamic response to shallow foundations via the simulation of the shake table experiment.

The damping conditions are given below and do not vary throughout the calculation. The dashpot coefficients of the beam elements are assumed to be proportional to the element stiffness matrix and 2% of the dashpot coefficient is taken into account. The damping of the macro element includes the radiation damping factors for an infinite elastic soil medium. Basically, the imaginary values of the dynamic impedance function (Gazetas, 1991) around resonance are chosen. Since the rocking motion is likely to be prominent, the resonance rocking frequency is approximated as 23.2 Hz via $\sqrt{K_r/J}/(2\pi)$, where J is the moment of inertia of the model pier footing.

However, the theoretical damping for rocking is much smaller than the values engineers typically take into ac-

count in seismic design for foundations. The theoretical damping approximately corresponds to a dashpot coefficient of 0.002, while the dashpot coefficient is often considered to be 0.1–0.3 in practice (Japan Road Association, 2002). When simulating the experimental results with the theoretical rocking dashpot coefficient, unrealistically large amplitudes of acceleration continued to appear in the calculation until the end of the excitation, indicating that the damping did not work effectively. Therefore, a rocking dashpot coefficient of 0.02 ($C_r = 1$ kN·s·m) is finally adopted throughout the present paper, which is made one-order larger than the theoretical value and is in the range of commonly used values. The values of the vertical, translational, and rocking dashpot coefficients are listed in Table 4.

Table 4. Dashpot coefficients of macro element

Vertical, C_v (kN·s/m)	130
Transitional, C_h (kN·s/m)	90
Rocking, C_r (kN·s·m)	1.0*

*Corresponding to a dashpot coefficient of 0.02

The measured horizontal acceleration time histories on the soil surface were applied to the macro element. No vertical motion on the soil surface was applied. The initial conditions are the same as those considered in the simulation of the monotonic loading experiment. Note

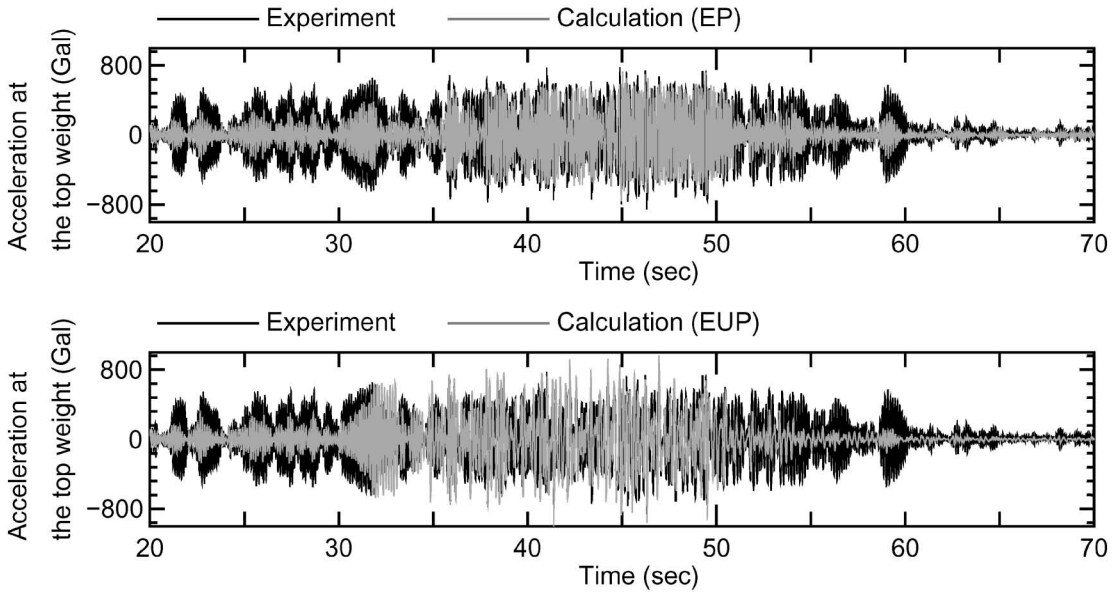

Fig. 23. Observed and calculated horizontal acceleration time histories at the top weight; Case 1

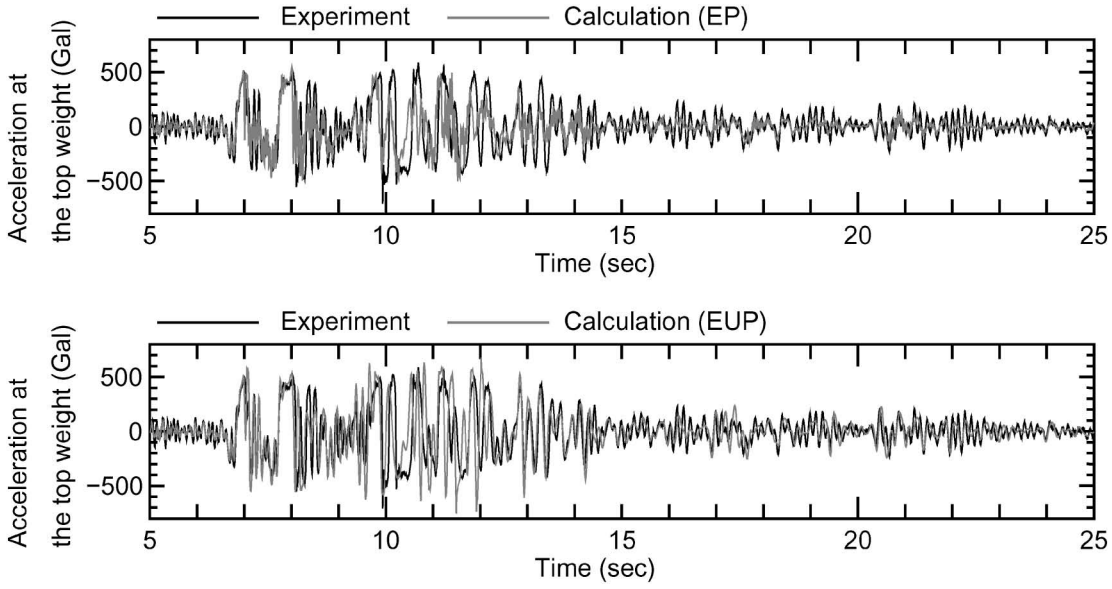

Fig. 24. Observed and calculated horizontal acceleration time histories at the top weight; Case 2

that the average residual settlements of the soil deposit at the end of the excitation were negligible in the experiment.

Figures 23 and 24 show the observed and calculated horizontal acceleration time histories at the top weight. In the experiments, acceleration was measured using accelerometers. The overall trends of the observed and calculated time histories are in good agreement. The fact that the peak acceleration amplitudes are predicted well indicates that the ultimate bearing capacity of the footing is satisfactorily predicted in the calculation. The results calculated with the EP and EUP macro elements are similar in terms of the prediction of the peak levels. The difference in the calculated results with the EP and EUP macro elements is that higher frequency components are included in the result with the EP macro element, because the EP macro element cannot give a degradation in the apparent elastic rigidity for rocking, as shown in the calculated results for the monotonic lateral loading experiment.

Figures 25 and 26 show the observed and calculated time histories of load eccentricity on the footing, $M/V/(B/2)$, together with the time histories of M and V, where the time windows include the times at which predominant acceleration amplitudes were input to the shake table in the experiment. Although the vertical

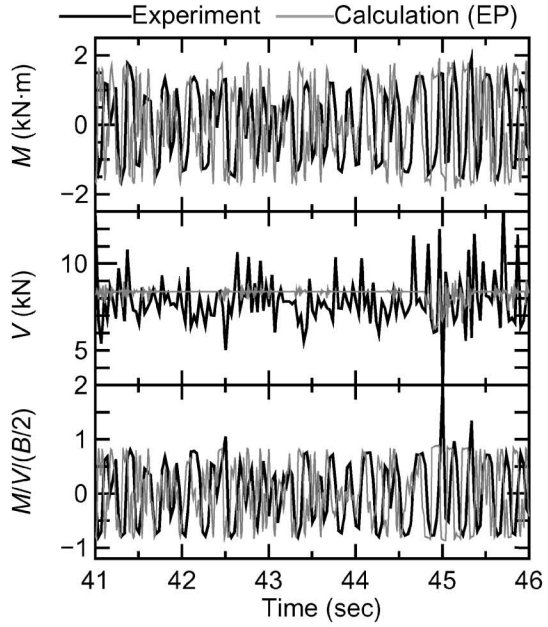

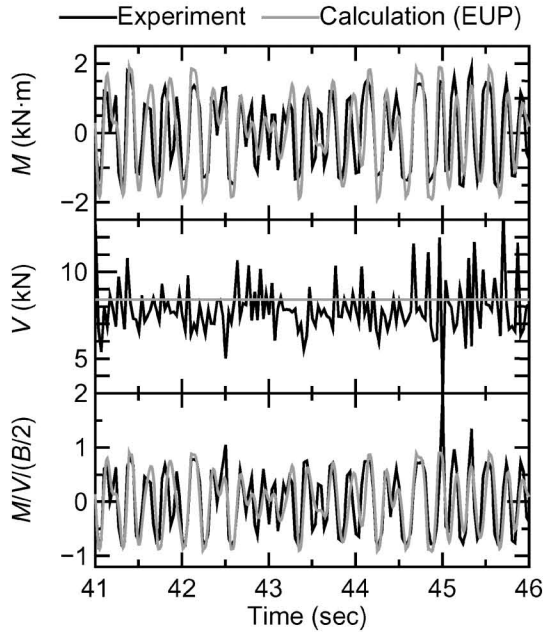

Fig. 25. Time histories of moment M, vertical load V and normalized moment $M/V/(B/2)$ at the base center of the footing for Case 1 (t = 41–46 sec)

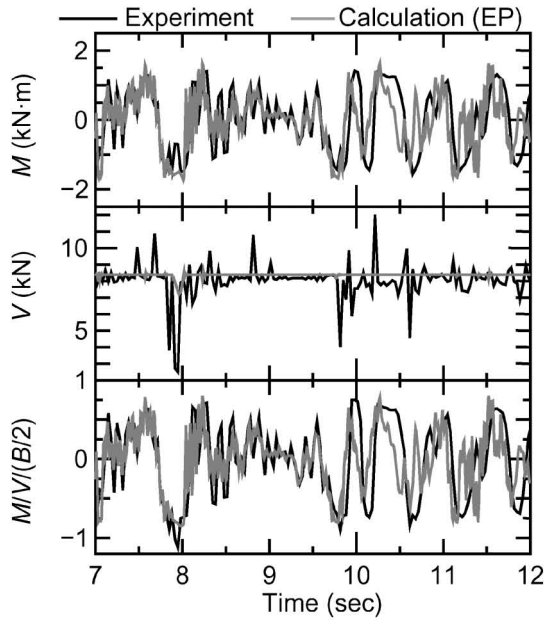

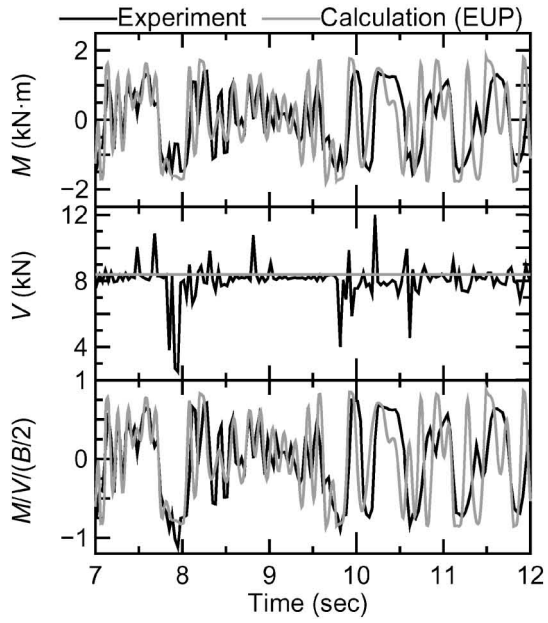

Fig. 26. Time histories of moment M, vertical load V and normalized moment $M/V/(B/2)$ at the base center of the footing for Case 2 (t = 7–12 sec)

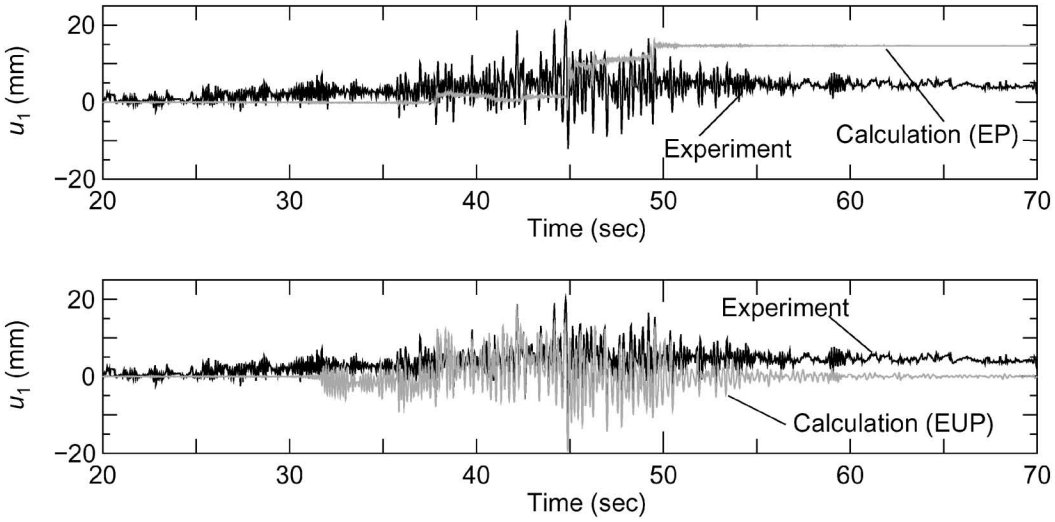

Fig. 27. Observed and calculated horizontal displacement time histories at the top weight; Case 1

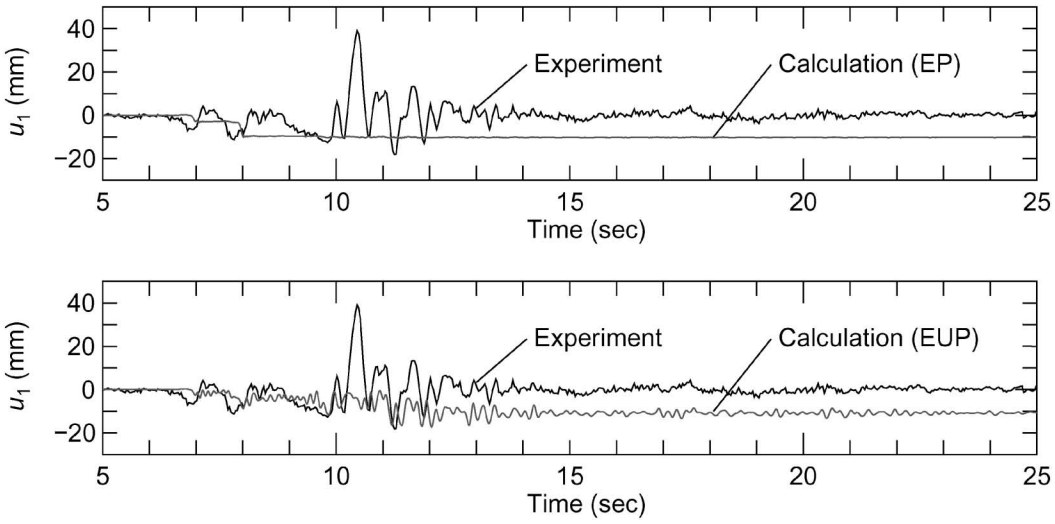

Fig. 28. Observed and calculated horizontal displacement time histories at the top weight; Case 2

force, V, does not vary in the calculation, both EP and EUP macro elements successfully predict the time histories of $M/V/(B/2)$ and M. The calculated amplitude at each peak is in good agreement with the experimental result, and phase characteristics, such as the timing at which each wave motion crosses the abscissa and reaches each peak, are successfully predicted. In particular, when using the EUP macro element, the calculated vibrations are as smooth as those observed in the experimental results.

Figures 27 and 28 show the observed and calculated time histories of the horizontal displacement at the top weight, u_1, where both EP and EUP macro elements are tested. Horizontal displacements of the model pier footing are estimated as the displacement relative to the observed horizontal displacement of the soil surface and observed displacements were captured from the VCR records. It appears that the EP macro element cannot respond to the dynamic horizontal vibration, which is a salient flaw of the EP macro element for the use of seismic design for structures. The result calculated with the EUP macro element agrees well with the experimental result for Case 1. Even for Case 2, the EUP macro element predicts the dynamic vibration of the horizontal displacement, although it underestimates the maximum displacement around an elapsed time of 10.5 s because the rocking-induced uplift in the experiment was extremely large.

In summary, as also suggested in a companion paper (Paolucci et al., 2008), the numerical results confirm that the incorporation of the uplift-induced degradation of rocking stiffness significantly improves the numerical prediction of the overall dynamic behavior of shallow foundations during large earthquakes.

Figures 29 and 30 show the observed and calculated time histories of the settlement at the base center of the footing, v/B, where the EUP macro element is used in the calculation. The settlement, v, is normalized by the foot-

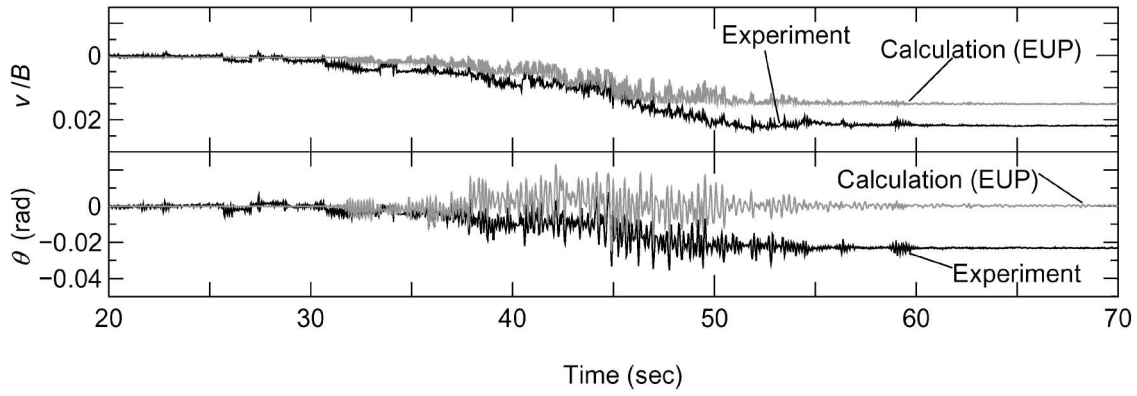

Fig. 29. Observed and calculated time histories of rotation and settlement at the base center of the footing, θ and v; Case 1

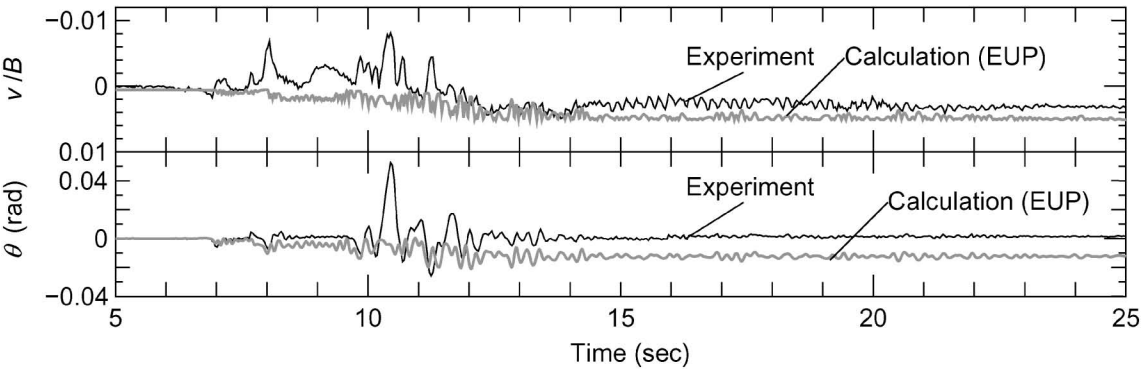

Fig. 30. Observed and calculated time histories of rotation and settlement at the base center of the footing, θ and v; Case 2

ing length, B. For reference, the time histories of the rotation at the base center of the footing, θ, are also plotted. The calculation predicts that the footing gradually settles together with the up-and-down motion, as seen in the experimental results. Corresponding to rotation, the vertical settlement also vibrates up and down. In the experiments, the accumulation of the settlement of the footing in Case 1 was clearly larger than that in Case 2, and the calculation can also predict such a tendency. The observed settlements were 10.62 mm (=2.12% of the footing length, B) for Case 1 and 1.89 mm (=0.38% of the footing length, B) for Case 2, while the calculated settlements were 7.91 mm (=1.58% of the footing length, B) for Case 1 and 2.48 mm (=0.50% of the footing length, B) for Case 2. The orders of calculated settlements agree with the experimental results. This indicates that the EUP macro element is capable of accounting for the seismic bearing characteristic, which varies with the number of cycles of the earthquake motions. In addition, when comparing the macro element examined in the companion paper (Paolucci et al., 2008), a clear improvement is found in the calculating accuracy of the residual rocking-induced settlement, which is one of the motivations of the present study.

It seems that there still is a need to improve the hysteresis rule for apparent elastic components of the M-θ relationship and work hardening rule. For example, for Case 1, the calculation cannot predict the irreversible rotation at the end of the excitation.

CONCLUDING REMARKS

The present paper has explored the macro element approach to simulate the nonlinear response and the accumulation of irreversible settlement of a shallow foundation subjected to a large earthquake. The present paper integrated a strain hardening macro element theory with an apparent degradation in the elastic rigidity of the rocking behavior associated with the footing uplift. The proposed macro element was then tested via the simulations of the experiments of model pier footings subjected to static monotonic horizontal-rocking loading and shake table loading. The results presented herein are summarized below:

1. The EUP macro element is useful for estimating the overall tendency of the load and displacement time histories of shallow foundations during earthquakes.
2. The prediction of the vibration frequency and hysteresis loop shapes in the rocking motion has clearly been improved when considering the uplift of the footing.
3. The macro element theory is capable of accounting for the bearing capacity and rocking-induced settle-

ments during earthquakes, while the theory was originally developed based on the results of a monotonic loading experiment.

4. The revised macro element is capable of predicting the change in accumulated settlements, which depend on the type of earthquake.

As a first approximation, for the sake of simplicity, we assumed that the vertical force does not change during earthquakes. However, it would be better to examine the appropriateness of this simplification, because there may be cases in which the variation in the vertical force applied to a footing cannot be ignored in the calculation. This is an area for future study. It is hoped that the present paper, the FORTRAN source code, and PWRI experimental results will help to improve the seismic design for shallow foundations.

ACKNOWLEDGMENTS

This research was conducted as part of the five-year joint research agreement between the Public Works Research Institute, Tsukuba, Japan, and Politecnico di Milano, Milan, Italy 2003–2007, on seismic design methods for bridge foundations and was supported in part by the Executive Program of Cooperation in the Fields of Science and Technology between the governments of Italy and Japan 2002–2006, Project No. 13B2.

REFERENCES

1) Cremer, C., Pecker, A. and Davenne, L. (2001): Modelling of nonlinear dynamic behaviour of a shallow strip foundation with macro-element, *Journal of Earthquake Engineering*, **6**(2), 175–211.
2) Cremer, C. and Pecker, A. (2002): Cyclic macro-element for soil-structure interaction: material and geometrical non-linearities, *International Journal for Numerical and Analytical methods in Geomechanics*, **25**, 1257–1284.
3) Fukui, J., Kimura, Y., Ishida, M. and Kishi, Y. (1999): An investigation on the response of shallow foundations to large earthquakes, *Technical Memorandum of PWRI*, Public Works Research Institute, (3627) (in Japanese).
4) Fukui, J., Nakatani, S., Shirato, M., Kouno, T., Nonomura, Y. and Asai, R. (2007): Experimental study on the residual displacement of shallow foundations during large earthquakes, *Technical Memorandum of PWRI*, Public Works Research Institute, (4027) (in Japanese).
5) Fukui, J., Nakatani, S., Shirato, M., Kouno, T., Nonomura, Y., Asai, R. and Saito, T. (2007): Large-scale shake table test on the nonlinear seismic response of shallow foundations during large earthquakes, *Technical Memorandum of PWRI*, Public Works Research Institute, (4028) (in Japanese).
6) Gajan, S., Kutter, B., Phalen, J., Hutchinson, T. and Martin, G. (2005): Centrifuge modeling of load-deformation behaviour of rocking shallow foundations, *Soil Dynamics and Earthquake Engineering*, **25**, 773–783.
7) Gazetas, G. (1991): *Foundation Engineering Handbook* (second edition, ed. by Fang, H. Y.), Chapter 15, Van Nostrand Reinhold.
8) Gottardi, G. and Butterfield, R. (1995): The displacement of a model rigid surface footing on dense sand under general planar loading, *Soils and Foundations*, **35**(3), 71–82.
9) Haya, H. and Nishimura, A. (1998): Proposition of design method of spread foundation considering large sale earthquake force, *JSCE Journal of Construction Engineering and Management*, (595/VI–39), 127–140 (in Japanese).
10) Honshu-Shikoku Bridge Authority (1990): *Draft Guidelines for the Seismic Design of the Kurushima Kaikyo Bridges* (in Japanese).
11) Houlsby, G. and Martin, C. (1993): Modelling of the behaviour of foundations of jack-up units on clay, *Predictive Soil Mechanics* (eds. by Houlsby and Schofield), Thomas Telford, 339–358.
12) Japan Road Association (2002): *Specifications for Highway Bridges*, Maruzen.
13) Meyerhof, G. G. (1953): The bearing capacity of foundations under eccentric and inclined loads, *Proc. 3rd ICSMFE*, **1**, Zurich, 440–445.
14) Motrasio, L. and Nova, R. (1997): Settlements of shallow foundations on sand: geometric effects, *Géotechnique*, **47**(1), 49–60.
15) Nakatani, S., Shirato, M. and Kouno, T. (2008): Development of a numerical model for the seismic nonlinear behavior and irreversible displacement of a shallow foundations, *PWRI Report*, Public Works Research Institute, (4101) (in Japanese).
16) Nova, R. and Montrasio, L. (1991): Settlement of shallow foundations on sand, *Géotechnique*, **41**(2), 243–256.
17) Okamura, M. and Matsuo, O. (2002): A displacement prediction method for retaining walls under seismic loading, *Soils and Foundations*, **42**(1), 131–138.
18) Okamura, M., Mihara, A., Takemura, J. and Kuwanoand, J. (2002): Effects of footing size and aspect ratio on the bearing capacity of sand subjected to eccentric loading, *Soils and Foundations*, **42**(4), 43–56.
19) Paolucci, R. (1997): Simple evaluation of earthquake-induced permanent displacements of shallow foundations, *Journal of Earthquake Engineering*, **1**(3), 563–579.
20) Paolucci, R., Shirato, M. and Yilmaz, M. (2008): Seismic behavior of shallow foundations: shaking table experiments vs. numerical modelling, *Earthquake Engineering and Structural Dynamics*, **37**(4), 577–595.
21) Shibata, T. and Sekiguchi, H. (1995): *Bearing Capacity of Soils*, Kashima Institute Publishing (in Japanese).
22) Shirato, M., Kouno, T., Asai, R., Nakatani, S., Fukui, J. and Paolucci, R. (2008): Large-scale experiments on macroscopic nonlinear behavior of shallow foundations subjected to strong earthquakes, *Soils and Foundations*, **48**(5), 673–692.
23) Vesic, A. S. (1991): *Bearing Capacity of Shallow Foundations*, Van Nostrand Reinhold, 121–147.